

Interest Point Detection for Reconstruction in High Granularity Tracking Detectors

B. Morgan

*Department of Physics,
University of Warwick,
Coventry, CV4 7AL, United Kingdom
E-mail: Ben.Morgan@warwick.ac.uk*

ABSTRACT:

This paper presents an investigation of the use of interest point detection algorithms from image processing applied to reconstruction of interactions in high granularity tracking detectors. Their purpose is to extract keypoints from the data as input to higher level reconstruction algorithms, replacing the role of human operators in event selection and reconstruction guidance. Simulations of $\nu_\mu + {}^{40}\text{Ar} \rightarrow \mu^- + p$ in a small liquid argon time projection chamber are used as a concrete example of a modern high granularity tracking detector. Data from the simulations are used to characterize the localization of interest points to physical features and the efficiency of finding interest points associated with the primary vertex and track ends is measured. A high degree of localization is found, with 93% of detected interest points found within 5mm of a physical feature. Working in two 2D projections, the primary vertex and both track ends are found in both projections in 85% of events. It is also shown that delta electrons can be detected.

KEYWORDS: liquid argon; time projection chamber; reconstruction; pattern recognition; feature detection; computer vision.

Contents

1. Introduction	1
2. Interest Point Detection using the Structure Tensor	2
3. Simulation of Detector, Events and Data	4
4. Detection and Analysis of Interest Points from Simulated Events	5
4.1 Localization of Interest Points	5
4.2 Efficiency of Detecting the Primary Vertex and Track End Points	7
4.3 Detection of Secondary Particles	8
5. Conclusions	9
6. Acknowledgements	10

1. Introduction

Bubble chambers are the classic example of a high granularity tracking detector, and provided a key tool for many discoveries in particle physics [1, 2]. The complex event topologies studied by these experiments and the limited computing power of the time presented a great challenge in reconstructing and characterizing the recorded interactions [3, 4]. Significant progress was made in fully automated measurement for very simple event topologies [5], yet more complex interactions still required a high degree of human input for pattern recognition and measurement guidance [6]. In these cases, an operator would examine the image on a scanning table, identifying events and marking keypoints such as vertices to provide guidance to the automated measurement system [7].

As electronic detectors took over from the bubble chambers, the general trend in tracking moved to trackers layered around a known vertex region with trajectories measured at a few sparse points with very high resolution. Pattern recognition techniques have correspondingly evolved to handle this data and complete automation has been achieved [8]. Yet significant interest has remained in high granularity tracking due the potential for robust particle identification and precise kinematics in a simple, homogeneous detector. The modern exemplar of such a detector is the Liquid Argon Time Projection Chamber (LAr-TPC) [9] which provides simultaneous tracking and calorimetry with millimetric granularity. Some reconstruction and pattern recognition techniques have been demonstrated for LAr-TPCs, but like bubble chambers these have used human-computer interaction to both select events and to guide the reconstruction [10, 11]. With the start of data-taking for ICARUS T600 [12] and ArgoNeut [13], significant interest has developed in fully automating reconstruction for LAr-TPCs, both to remove operator bias and to handle the large datasets expected.

The use of human-computer techniques in LAr-TPC reconstruction has arisen from many of the same challenges faced by bubble chamber analyses. LAr-TPCs are targeted at neutrino oscillation and cross-section studies at the few GeV scale [12, 13, 14], and also nucleon decay searches [15]. The event classes to be reconstructed thus consist of multiple vertex hadron decays and electromagnetic/hadronic showers, giving a complex pattern recognition task. Like a bubble chamber, interactions can occur anywhere within the TPC volume, giving no clue to primary and secondary vertex locations and consequently complicating initialization of any pattern recognition algorithm. Unlike the separated tracking and calorimeter components of typical collider detectors, tracks and showers occur together in a LAr-TPC, leading to a complex “track” recognition task that must separate and cluster both tracks and showers. These tasks of vertex/keypoint identification and shower/track separation have not yet been automated in LAr-TPC reconstruction and are therefore a key goal for any fully computational approach.

Like bubble chamber photographs, LAr-TPC data represents an image of the pattern of ionization left by charged particles, with reconstruction efforts concentrating on the use of two 2D (pixel) images projected from the underlying 3D (voxel) image. Pattern recognition in images is a well established subfield of Image Processing, to which bubble chamber analyses contributed through the Hough Transform for identifying straight line features [16]. Many other types of features can be detected in images, and perhaps the most well known class of feature detection algorithms are the interest point detectors [17]. An interest point may be defined as a point in an image which differs in a mathematically describable way from its local neighbourhood. Whilst many mathematical descriptors have been developed, the most common and frequently used are those based on local intensity differences. This concept was first introduced by Moravec [18], who defined “points of interest” as points in an image where the intensity varied strongly in all directions. Interest point detection based on Moravec’s concept is also known as “corner detection” as corner like structures display the strong directional intensity variance picked out by the algorithms. As structures like decay vertices in a LAr-TPC image essentially form a corner, this motivates an application of interest point detection to identify the position of vertices and other keypoints for use by downstream reconstruction algorithms. This approach does not seek to fit a vertex or keypoint location, rather, it aims to provide a rough location to guide higher level pattern recognition, replacing the role of a human operator.

In this paper, intensity variation-based interest point detection is applied to identify keypoints in $\nu_\mu + {}^{40}\text{Ar} \rightarrow \mu^- + p$ events simulated in a small LAr-TPC. Section 2 describes the quantification of intensity variation in terms of the structure tensor and shows how this is used to define an interest point response function. Section 3 describes the simulation of the detector, input events and output data. Analysis of this data to extract interest points in two 2D images is discussed in Section 4, with results on the localization of interest points with physical features and the efficiency of identifying known keypoints. A summary of these results and future directions is given in Section 5.

2. Interest Point Detection using the Structure Tensor

Interest point detection using intensity variations in an image was first introduced by Moravec [18], who defined “points of interest” as points where the intensity $I(x,y)$ varies strongly in all directions. Moravec’s technique quantifies the local intensity variation $M(x,y)$ around each pixel by finding

the minimum difference in intensity between a small window centred on the pixel and the same window shifted by a few pixels along each of the eight cardinal plus ordinal directions. Large values of $M(x,y)$ thus correspond to points with large intensity variations in all directions, with interest points hence identified and extracted as the coordinates of local maxima of $M(x,y)$.

Harris & Stephens [19] removed the directional quantization inherent in Moravec’s algorithm by expanding the intensity variation equation using a first order Taylor series. They showed that the intensity gradient structure local to a point is encapsulated by the structure tensor (or second moment matrix) averaged over the neighbourhood of the point:

$$S(x,y) = g(\sigma_s) * \begin{bmatrix} I_x(x,y)^2 & I_x(x,y)I_y(x,y) \\ I_x(x,y)I_y(x,y) & I_y(x,y)^2 \end{bmatrix} \quad (2.1)$$

where $*$ denotes convolution, $I_{x(y)}$ is the partial derivative of the image with respect to $x(y)$ and g is a Gaussian window

$$g(\sigma) = \exp\left(\frac{-(x^2 + y^2)}{2\sigma^2}\right). \quad (2.2)$$

which is convolved with the second moment matrix to provide averaging and reduce noise [19]. Whilst Harris & Stephens used a Prewitt filter to calculate the derivatives, modern implementations recommend a Gaussian derivative filter to improve rotational invariance (S is fundamentally rotationally invariant, but certain derivative operators are not) and signal-to-noise [20]. Use of a Gaussian derivative filter provides differentiation of the image as

$$I_x(x,y) = g(\sigma_d) * \frac{\partial I(x,y)}{\partial x} = \frac{\partial g(\sigma_d)}{\partial x} * I(x,y). \quad (2.3)$$

The standard deviations σ_s for averaging and σ_d for differentiation are usually chosen to be the same, though this is not required.

Equation 2.1 provides the basis for many interest point detectors (see for instance [17]) because its eigenvalues and eigenvectors describe the intensity variation local to any point in the image. If we consider a line, i.e. a particle track-like object, then the gradient in intensity will be small along the line and large perpendicular to the line. Consequently, $S(x,y)$ for (x,y) along the line will have one large eigenvalue and one small. In contrast, if we consider two lines meeting in a ‘V’, i.e. a decay vertex-like structure, then the intensity gradient will be large in all directions at points close to the ‘V’ vertex. Thus at these points, $S(x,y)$ will have two large eigenvalues. Functions of $S(x,y)$ can therefore be constructed to produce a feature response image $R(x,y) = f(S(x,y))$ whose local maxima will correspond to the interest points of a particular type.

The best known, and most widely used, feature response function is that proposed by Harris & Stephens (sometimes known as the Plessey operator) [19], with

$$R_{HS}(x,y) = \det(S(x,y)) - k\text{Tr}^2(S(x,y)) \quad (2.4)$$

where k is a tunable parameter. Since the determinant(trace) corresponds to the product(sum) of the eigenvalues of S , R_{HS} will be large if both eigenvalues are large. Thus maxima of R_{HS} correspond to points with a corner-like, i.e. vertex-like, structure.

However, the extra degree of freedom in R_{HS} from the k parameter complicates the characterization of interest point detection for LAr-TPC reconstruction. To simplify this analysis, another common feature response function proposed by Förstner [21] and Noble [22] is used:

$$R_N(x,y) = \begin{cases} \frac{\det(S(x,y))}{\text{Tr}(S(x,y))} & \text{if } \text{Tr}(S) > 0 \\ 0 & \text{if } \text{Tr}(S) = 0 \end{cases} \quad (2.5)$$

Like the Harris & Stephens response function, R_N will have maxima at corner-like structures in the image, and hence interest points are extracted as the coordinates of these maxima.

Interest points for reconstruction in a LAr-TPC will clearly be features such as decay vertices, interaction points and track stop points. As all of these can be built from primitive line and ‘V’ shapes, processing a LAr-TPC image with Equation 2.5 should lead to these points being picked out as maxima in the resulting response image. It should be noted that interest point extraction is not applied here as a fit to the locations of, e.g., vertices, as interest points will only be localized by the extraction to the nearest pixel. Whilst techniques exist for sub-pixel resolution, the smoothing and gradients used in structure tensor based approaches can displace maxima in the response from the true feature location [17]. Rather, interest point detection in LAr-TPC reconstruction should be viewed as replacing the role of a human operator in picking out, e.g., rough vertex locations and other key points for use by higher level pattern recognition algorithms.

3. Simulation of Detector, Events and Data

The Geant4 toolkit [23] was used to model a simple LAr-TPC as a stainless steel cylinder of 1m radius and 2m height, filled with natural argon in the liquid state. All material properties were taken from the NIST database built in to Geant4. Standard electromagnetic and decay processes were modelled for all particles. To provide a simple and well defined final state topology for characterizing the interest point detector, no hadronic decay or inelastic processes were modelled. The application of interest point detection for hadronic decay chains and showers will be the subject of a future publication.

The GENIE [24] software package was used to generate a 1000 event sample of quasi-elastic charged current (QEL-CC) $\nu_\mu + {}^{40}\text{Ar} \rightarrow \mu^- + p$ events. The input ν_μ spectrum was monoenergetic with an energy of 0.7GeV, chosen to match that around the peak flux of the JPARC beam [25]. The neutrinos were directed in a beam along the x-axis through the centre of the TPC vessel. At the chosen energy, events with a pure $\mu^- + p$ final state comprise around 60% of all GENIE-generated QEL-CC events.

The liquid argon volume was divided into $1 \times 1 \times 1\text{mm}^3$ voxels, giving a slightly higher granularity than current detectors. This allows a conservative study, as higher granularities are more challenging due to the greater detail present. All primary and secondary particles were tracked through the voxels down to zero energy or until they left the TPC volume. Energy deposits by charged particles passing through the voxels were tallied into a map between voxel coordinates (i, j, k) and the total energy deposited in that voxel, E . Together with this voxel map of the energy deposits, the positions of physical feature points were recorded, specifically the primary vertex, stop/decay/exit points of the primary muon and proton, and the creation and stop/exit points of

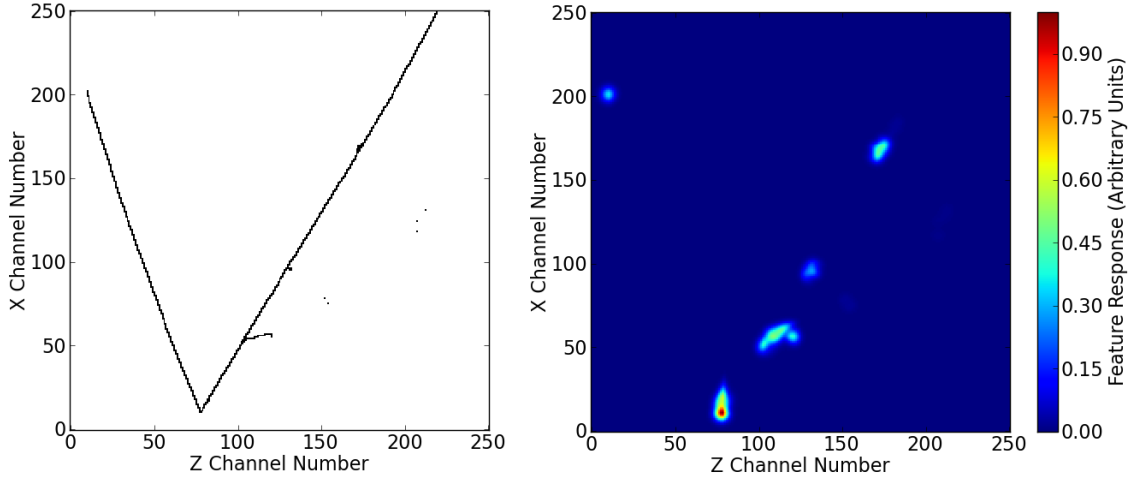


Figure 1. XZ projection images of hits (*left*) from a $\nu_\mu + {}^{40}\text{Ar} \rightarrow \mu^- + p$ event (μ^- right, p left), and the resultant response image R_N for the hits (*right*). Channel numbers give the pixel coordinates, with 1 channel equivalent to a spatial dimension of 1mm. The primary vertex, proton stopping point and delta electrons are clearly picked out as intensity peaks in the response image.

delta electrons. No modelling of the readout system or hit/voxel reconstruction from raw data was performed as this is highly experiment-specific.

4. Detection and Analysis of Interest Points from Simulated Events

In line with other LAr-TPC reconstruction efforts, the analysis of interest points uses two 2D projections of the 3D voxel data. For each event, the 3D energy deposition map was projected to two 2D images with $1 \times 1 \text{mm}^2$ pixels in the xz and xy planes perpendicular to the neutrino beam. Each non-zero pixel was set to a value of 1 to remove energy deposition information. Whilst this reduces the total information content in the image, it specifically highlights the geometric structure of the event which is of primary importance in locating vertex and other physical interest points. Leaving the energy information in results in a biased response to regions of high dE/dx contrast, masking the more important geometric information. The feature response images $R_N(x, y)$ and $R_N(x, z)$ were calculated for each input image using Equations 2.1, 2.3 and 2.5. Derivative and smoothing filter widths were chosen as $\sigma_d = \sigma_s = 2.5 \text{mm}$. Figure 1 shows an example event and the resultant response image.

Interest points were identified as local maxima of the R_N images, with the pixel coordinates and R_N value of these maxima extracted using a non-maximum suppression filter. This filter used a square window of width 10mm, chosen to match twice the total smoothing/derivative width, $\sigma_d + \sigma_s$, the rough scale of peaks in R_N for isolated structures. The resultant sets of interest points, (x, y, R_N) and (x, z, R_N) , for each projected image were finally thresholded to select only those points with a value of R_N within 90% of the maximum R_N value in the set.

4.1 Localization of Interest Points

If interest points extracted from the data are to be useful in higher level pattern recognition algo-

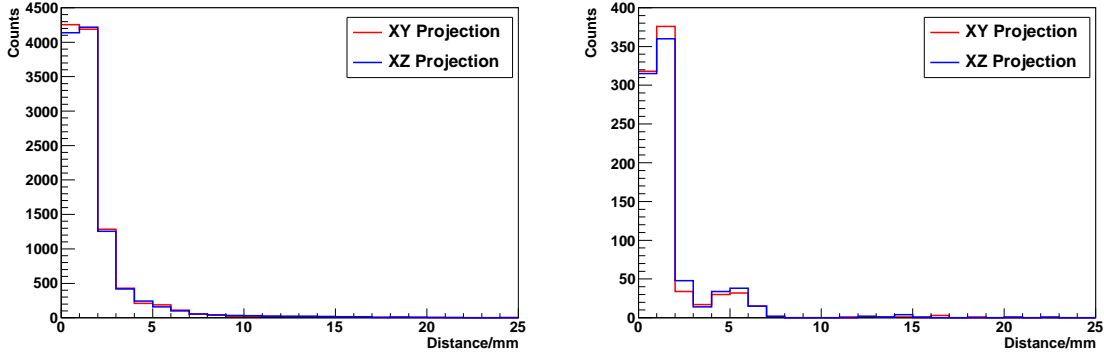


Figure 2. Distributions of distances between all detected interest points and nearest physical feature (*left*), and interest points nearest to the primary vertex and the primary vertex itself (*right*), for the *xy* and *xz* projections.

rithms, they should be closely related in space to actual physical features. To characterize this, the nearest (projected) physical point to each extracted interest point was identified from the simulation outputs, with the distance between the points being measured together with the classification of the physical point. The distribution of these distances in each projection is shown in Figure 2 for all interest points and for the subset of interest points whose nearest physical point was the primary vertex.

It can be seen from Figure 2 that the distance distributions are peaked at small distances, indicating that the detected interest points are correlated with physical features. Both distributions are the same, within statistical errors, for both projections which is expected as both planes contain the beamline. The localization of physical features by detected interest points is good, 93% of all interest points being within 5mm of a physical feature, and 89% of the interest points closest to the primary vertex being within 5mm of the vertex. Clearly, the detected interest points have high correlation with physical features and are thus of potential use as seeds or keypoints by other pattern recognition algorithms. Algorithmic and physical effects contribute to the broadening of the distance distributions, though it is again emphasized that the extracted feature points do not represent a fit to a physical location, e.g. a primary vertex.

Due to the use of gradients in structure tensor approaches, maxima in the response function may be displaced from the physical feature, particularly at ‘T’ junctions [26]. This effect only contributes to the broadening below ~ 5 mm as this is the typical width of peaks in the response function, as seen in Figure 1. At larger distances, ‘noise’ features contribute to the broadening due to the relatively low response threshold chosen. Tuning of the derivative/smoothing filter widths and threshold parameters may help to reduce these effects, and this is left for concrete implementations as it will be sensitive to the event topology and the behaviour of other pattern recognition algorithms making use of the detected points. The shoulder at ~ 5 mm in the distance distribution for interest points closest to the primary vertex arises from interference between the gradients of the primary vertex and nearby delta electrons. This leads to a merging of the resultant peaks in the response function and consequently a displacement of the measured interest point location(s) from the primary vertex and delta electron start/end. This will occur on scales of the overall width of the

Measure	xy Efficiency	xz Efficiency
Vertex Found Directly	$(81.8 \pm 2.9)\%$	$(82.0 \pm 2.9)\%$
Feature $< 5\text{mm}$ from Vertex	$(90.5 \pm 3.1)\%$	$(91.1 \pm 3.1)\%$
Feature $< 5\text{mm}$ from Both Primary Track Ends	$(90.3 \pm 3.1)\%$	$(88.8 \pm 3.0)\%$

Table 1. Efficiencies for finding primary vertex and muon/proton track ends in the two image projections. Uncertainties were calculated as the Poisson error on the counted number of events in the 1000 event sample, and should be read as counting errors rather than strict percentages.

derivative/smoothing kernels used, leading to maxima in R_N , and hence identified interest points, displaced on scales of $\sim 5\text{mm}$.

4.2 Efficiency of Detecting the Primary Vertex and Track End Points

Whilst Section 4.1 shows physical features to be located accurately, the detection algorithm must also find them at high efficiency if they are to be useful to higher level pattern recognition algorithms. In particular, the primary vertex and primary track end points may be key for certain track finding algorithms. To characterize the efficiency of finding an interest point related to the primary vertex, the number of events with an interest point classified as closest to the primary vertex (see Section 4.1) was counted for each projection. This number divided by the total number of events gives the efficiency of directly finding an interest point related to the primary vertex, and is given in Table 1 for each projection.

Whilst this efficiency is relatively high, it underestimates the actual efficiency available to a real analysis. The interference from delta electrons discussed in Section 4.1 means that an interest point related to the primary vertex may be classified as closest to a secondary by the nearest neighbour analysis. However, a real analysis has no knowledge of the underlying physical features, and higher level algorithms will only require a rough localization of the primary vertex and other points. It is therefore more useful to ask “is there an interest point within a distance d of the primary vertex?”. Whilst d is somewhat arbitrary, $\sim 5\text{mm}$ was chosen as this provides good localization and matches the scale over which interference from delta electrons occurs. The number of events with an interest point within 5mm of the primary vertex was counted for each projection and divided by the total number of events, the results being shown in Table 1. This analysis was repeated to determine the efficiency of finding an interest point within 5mm of one or both of the muon and proton track ends, these results also being shown in Table 1.

Both the primary vertex and muon/proton track ends are found with an efficiency of $\sim 90\%$ in both projections. Events with no interest points close to the vertex or tracks ends were visually scanned to try and identify reasons for the failure. The major reason for failure to find the primary vertex was a large opening angle between the muon and proton leading to local maxima in R_N below threshold. A few events were also observed to have high energy delta electrons close to the vertex that completely washed out the response from the vertex. With the muon/proton track ends, failure to find one or both was caused by short proton tracks, projection of the tracks with very small (projected) opening angle and again some delta electron contamination. These are effects

Measure	Efficiency
Vertex Found In One or Both Projections	$(96.2 \pm 3.1)\%$
Vertex Found In Both Projections	$(85.4 \pm 3.0)\%$
At Least One Track End In One or Both Projections	$(100.0 \pm 3.2)\%$
At Least One Track End In Both Projections	$(99.9 \pm 3.2)\%$
Both Track Ends Found In One or Both Projections	$(95.3 \pm 3.1)\%$
Both Track Ends Found In Both Projections	$(85.2 \pm 3.0)\%$

Table 2. Efficiencies for detecting an interest point $< 5\text{mm}$ from the primary vertex and muon/proton track ends in combined image projections. Uncertainties were calculated as the Poisson error on the counted number of events in the 1000 event sample, and should be read as a counting error rather than strict percentages.

of the underlying physics though, and overall the primary vertex and muon/proton track ends are found with excellent efficiency.

No matching of the two sets of 2D interest points to reconstruct 3D points is performed, but we can measure the efficiency for finding a feature in one or both projections. Table 2 shows combined efficiencies for finding an interest point $< 5\text{mm}$ from the primary vertex or muon/proton tracks ends in one or both projections. Compared with the $\sim 90\%$ efficiency for finding the primary vertex/track ends in a single projection, the $\sim 85\%$ combined efficiency is somewhat lower yet still performant.

It should however be possible to develop techniques for reconstructing 3D interest points from the two sets of 2D points. One could project the interest points as lines through the volume and find intersections and/or close approaches, but it may be better to perform a maximisation of the combined $R(x_1, x_2)$ response images. However, the optimum solution would be to detect interest points directly from the full 3D voxel data as this contains the maximum information. Equation 2.1 for the structure tensor extends naturally to three dimensions, but the extra degree of freedom means suitable response functions $R(x, y, z)$ are more sensitive to the exact structures being searched for. Early work has identified several potential candidates for $R(x, y, z)$ to identify vertex-like structures, and these will be reported in a future publication.

4.3 Detection of Secondary Particles

Whilst the primary vertex and track ends are the major key points that higher level track finding algorithms would find useful, delta electron start/end points may also be needed. If the detector resolves these into separate tracks, certain track finding algorithms, especially those operating locally hit by hit, may need these interest points in order to identify branching points.

Delta electrons can appear as ‘T/Y’ structures and are hence detectable as interest points, as can be seen in Figure 1. Their relatively low energy leads to a wide variance in structure however, and hence their detectability as interest points is strongly dependent on whether they clearly branch from their parent or simply merge into it.

Figure 3 shows the distribution of the fraction of all delta electrons in each event found as interest points. Clearly, delta electrons can be detected, but only a relatively small fraction of the total are picked out. This reflects the variance in delta electron structure rather than a failure

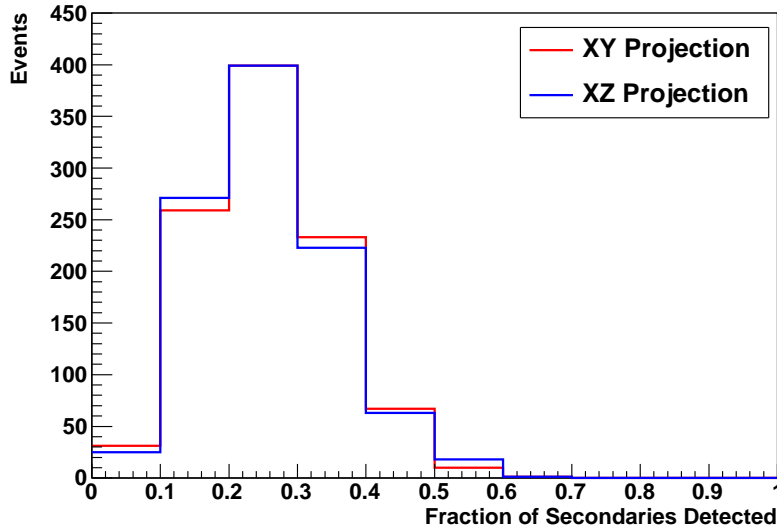


Figure 3. Distribution of per-event fraction of found secondary start/end points in the two image projections.

of the interest point detection, and should not be taken as a direct measure of the efficiency for finding delta electrons. That measurement requires knowledge of the downstream reconstruction algorithm(s) as the efficiency in this case would be quantified as the fraction of delta electrons *relevant to the downstream algorithm* that were detected. Not all delta electrons will be relevant to downstream algorithms, e.g. if they merge into the parent track. This study is left to later implementations of interest point detection in a full reconstruction chain.

5. Conclusions

This work has studied the application of a structure tensor based interest point detection algorithm to find primary vertices and track end points in neutrino charged current events recorded by a LAr-TPC. Interest point detection replaces the role of a human operator in selecting keypoints for use by higher level reconstruction, potentially providing a key part of a fully automated framework for reconstruction.

A sample of charged current events was simulated in a Geant4 modelled LAr-TPC, with physical interest points and a voxel image of the energy deposition recorded. Two dimensional images were created from the voxel image to match the reconstruction approach of ICARUS and ArgoNeut, with each image analysed with the Noble response function to extract interest points. It was found that the extracted interest points strongly correlate in position with physical features, with 93% of interest points being within 5mm of a physical feature in both projections. Noise, gradient based effects, and interference between nearby physical features cause a spread in the distribution of distances between interest points and underlying physical features. Better localization may be possible by tuning the derivative/averaging kernel widths used in calculation of the structure tensor. Nevertheless, the localization achieved is likely to be sufficient for most applications.

The efficiency with which interest points related to the primary vertex and track ends were found was also measured. Initially, the criterium for finding the primary vertex was taken as having an interest point whose nearest physical feature was the primary vertex. This resulted in $\sim 82\%$ of events finding the primary vertex, independent of the projection. It was recognized that real applications would not need such a strict criterium, since they simply require an interest point to be found close to the primary vertex. Further analysis showed that $\sim 91\%$ of events had an interest point within 5mm of the primary vertex, independent of the projection. The increase in efficiency arises from delta electrons close to the vertex interfering with the response, resulting in the nearest neighbour analysis classifying the interest point as a secondary, even though it is very close to the vertex. An identical analysis showed that $\sim 90\%$ of events found interest points within 5mm of both the muon and proton track ends, independent of projection. Whilst no 3D reconstruction of interest points from the two sets of 2D points was attempted, the efficiency analyses were combined to find the efficiencies for finding the primary vertex and track ends in either or both projections for the same event. This showed that the primary vertex or both track ends are found in both projections in $\sim 85\%$ of events. If real applications require better localization of interest points related to the primary vertex and tracks ends, this efficiency would decrease.

The application of interest point detection to identify delta electrons was studied, with 10-60% of secondaries detected as interest points in each projection. Clearly, delta electrons can be detected as interest points, but it is noted that this number does not represent an efficiency for detection as it does not distinguish secondaries that will be relevant to reconstruction, e.g. as a separate track, from those that simply merge into the main track. This study is left to actual applications with a defined downstream algorithm.

Clearly, interest point detection provides an accurate and efficient method for extracting physics-based points of potential use by other reconstruction algorithms. Whilst this work has concentrated on their application to neutrino interactions in a LAr-TPC, any detector with high granularity read-out and complex event topologies may find the technique useful. The initial implementation presented has worked with two 2D projections of the underlying 3D voxel data to give direct application to the reconstruction techniques already implemented for LAr-TPCs. However, the structure tensor approach to interest point detection should extend naturally to 3D, potentially giving improvements in localization and efficiency from the extra information available. Work has identified several suitable functions of the structure tensor for identifying tracks and vertices in 3D, and will be reported in a future publication.

6. Acknowledgements

The author is supported by STFC, and is grateful to Yorck Ramachers, Gary Barker and Paul Harrison for useful discussions. The use of the SciPy package [27] in the implementation of the interest point detection algorithms is acknowledged.

References

- [1] G. E. Kalmus, *Recent advances in bubble chamber physics, Reports on Progress in Physics* **36** (Aug., 1973) 961–1072.

- [2] G. Giacomelli, *Introduction to the Workshop "30 years of bubble chamber physics"*, *ArXiv Physics e-prints* (Apr., 2006) [physics/0604152].
- [3] P. Villemoes, *Data processing in bubble chamber experiments*, in *Proceedings of the 1970 CERN Computing and Data Processing School*, pp. 105–206, 1970.
- [4] M. Mermikides, *Data analysis for bubble chambers and hybrid systems.*, Tech. Rep. CERN-DD-80-31, CERN, Dec, 1980.
- [5] W. Allison *et. al.*, *Automatic scanning and measurement of bubble chamber film on POLLY II*, *Nuclear Instruments and Methods* **84** (1970), no. 1 129 – 137.
- [6] S. J. Barish *et. al.*, *Study of neutrino interactions in hydrogen and deuterium: Description of the experiment and study of the reaction $\nu + d \rightarrow \mu^- + p + p_s$* , *Phys. Rev. D* **16** (Dec, 1977) 3103–3121.
- [7] J. C. Gouache, *Description and status report of the ERASME system.*, Tech. Rep. CERN-DD-74-15, CERN, Geneva, May, 1974.
- [8] R. Mankel, *Pattern recognition and event reconstruction in particle physics experiments*, *Reports on Progress in Physics* **67** (Apr., 2004) 553–622, [physics/0402039].
- [9] C. Rubbia, *The liquid-argon time projection chamber: a new concept for neutrino detectors*, Tech. Rep. CERN-EP-INT-77-8, CERN, Geneva, 1977.
- [10] A. Martinez de la Ossa, *Study of accelerator neutrino interactions in a liquid argon TPC*, *ArXiv High Energy Physics - Experiment e-prints* (Mar., 2007) [hep-ex/0703026].
- [11] A. Ankowski *et. al.*, *Energy reconstruction of electromagnetic showers from π^0 decays with the ICARUS T600 Liquid Argon TPC*, *ArXiv e-prints* (Dec., 2008) [arXiv:0812.2373].
- [12] A. Menegolli and I. Collaboration, *Status of the ICARUS T600 detector at the LNGS*, *Journal of Physics Conference Series* **203** (Jan., 2010) 012107.
- [13] M. Antonello, *ArgoNeuT and MicroBooNE: LAr-TPC's at Fermilab*, in *American Institute of Physics Conference Series* (D. Kaplan, M. Goodman, & Z. Sullivan, ed.), vol. 1222 of *American Institute of Physics Conference Series*, pp. 257–261, Mar., 2010.
- [14] F. Cavanna, *The liquid argon tpc technology for precise (quasi-elastic) neutrino cross-sections reconstruction*, *Acta Physica Polonica B* **40** (2009) 2637–2646.
- [15] A. Bueno *et. al.*, *Nucleon decay searches with large liquid Argon TPC detectors at shallow depths: atmospheric neutrinos and cosmogenic backgrounds*, *Journal of High Energy Physics* **4** (Apr., 2007) 41, [hep-ph/0701101].
- [16] P. Hough, *Machine Analysis of Bubble Chamber Pictures*, in *Proceedings of the International Conference on High Energy Accelerators and Instrumentation*, pp. 554–556, 1959.
- [17] T. Tuytelaars and K. Mikolajczyk, *Local invariant feature detectors: a survey*, *Found. Trends. Comput. Graph. Vis.* **3** (2008), no. 3 177–280.
- [18] H. Moravec, *Obstacle Avoidance and Navigation in the Real World by a Seeing Robot Rover*, Tech. Rep. CMU-RI-TR-3, Carnegie-Mellon University, Robotics Institute, Sep, 1980.
- [19] C. Harris and M. Stephens, *A Combined Corner and Edge Detector*, in *Proc. Alvey Vision Conf.*, pp. 147–152, University of Manchester, 1988.
- [20] C. Schmid, R. Mohrand, and C. Bauckhage, *Comparing and evaluating interest points*, in *ICCV '98: Proceedings of the Sixth International Conference on Computer Vision*, (Washington, DC, USA), p. 230, IEEE Computer Society, 1998.

- [21] W. Förstner, *A feature based correspondence algorithm for image matching*, in *International Archives of Photogrammetry and Remote Sensing*, vol. 26, pp. 150–166, 1986.
- [22] A. Noble, “Descriptions of Image Surfaces.” PhD thesis, Department of Engineering Science, Oxford University, 1989.
- [23] S. Agostinelli *et. al.*, *Geant4 - a simulation toolkit*, *Nuclear Instruments and Methods in Physics Research Section A: Accelerators, Spectrometers, Detectors and Associated Equipment* **506** (2003), no. 3 250 – 303.
- [24] C. Andreopoulos *et. al.*, *The GENIE Neutrino Monte Carlo Generator*, *Nucl. Instrum. Meth.* **A614** (2010) 87–104, [[arXiv:0905.2517](https://arxiv.org/abs/0905.2517)].
- [25] M. Besnier and the T2K collaboration, *The contribution of near detectors to the t2k neutrino measurements*, *Journal of Physics: Conference Series* **203** (2010), no. 1 012105.
- [26] S. Smith, “Extracting Information from Images.” First Year D.Phil Report, Robotics Research Group, Department of Engineering Science, Oxford University, June, 1990.
- [27] E. Jones, T. Oliphant, P. Peterson, *et. al.*, *SciPy: Open source scientific tools for Python*, 2001-2010.